One Simple and Accurate Magnetic Equivalent Circuit Model for Electromagnetic Modeling of Synchronous Reluctance Motors

Farhad Rezaee-Alam[*1] and Abbas Nazari Marashi[2]

Departement of Electrical Engineering, Lorestan University, 68151-44316, Khorramabad, Lorestan, Iran, +989166591727, rezaee.fa@lu.ac.ir

Electrical Machine Research Group, ACECR, Khajeh Nasir Toosi University of Technology Branch, 16317-14191, Tehran, Iran, +989123416452, a_nazari@acecr.ac.ir

Abstract

This paper proposes an accurate magnetic equivalent circuit (MEC) model for synchronous reluctance motors (SynRMs) which is including the limited number of permeances in air-gap, and iron parts of stator and rotor. In proposed approach, the complex geometry of SynRM is divided into some parts, and the conformal maps are then used to calculate the permeance of relevant part in different paths. The conformal maps such as Schwartz-Christoffel (S-C) mapping is used to transform the complex geometry of different parts of SynRM into the canonical geometry in rectangle form. The permeance in relavant direction is then easily calculated in canonical geometry. It should be noted that the permeance is maintained while mapping the geometry from the physical domain into the canonical domain. After calculating the linear and non-linear permeances, the non-linear system of equations is created through writing the magnetic equation in different nodes of motor geometry. An iterative method is then used to solve the system of non-linear equations, to determine the scalar magnetic potential in all magnetic nodes, and to calculate the motor performance. In final, the accuracy of proposed MEC model is verified through comparing with corresponding results obtained from finite element method (FEM) and experiment set-up.

Index Terms: air-gap; flux barrier; magnetic equivalent circuit (MEC); permeance; schwartz-christoffel (S-C) mapping; synchronous reluctance motor (SynRM); Torque.

1. Introduction

The synchronous reluctance motors (SynRMs) have found wide industrial applications to replace induction motors due to having high torque density, fault tolerance, high flux-weakening, and so on [1]. For this reason, the accurate electromagnetic modeling is necessary for design and analysis of SynRMs. Finite element method (FEM) is the most famous technique for accurate modeling and analysis the SynRMs [1-4]. However, FEM is a time-consuming technique and it is better only used in final stage for verifying the analytical results. To this end, some analytical techniques have been used to model and analysis the SynRMs, such as the winding function theory (WFT) [5-7], the magnetic equivalent circuit (MEC) model [8-10], and conformal mappings [8-9]. Approximate analytical models have been also introduced to calculate the electromagnetic torque of SynRMs [11-13]. The saturation factors obtained through MEC model have been used in [13] to calculate the air-gap magnetic field of SynRMs while considering the magnetic saturation. In [5-6], the air-gap function has been calculated approximately for modeling and analysis the SynRMs by using WFT. In [8-9], the permeances of flux barriers were calculated by using the conformal maps for electromagnetic modeling the SynRMs by using the MEC model. In fact, few analytical models have been introduced for analysis the SynRMs, and FEM has been the main technique to study the performance of SynRMs. The main reason for this claim is the complicated geometry of the rotor of SynRMs.

To analytically solve this problem, one simple and accurate MEC model is presented in this paper for electromagnetic modeling the SynRMs, which helps from the conformal maps to calculate all permeances of iron parts, flux barriers, and air-gap region of SynRMs. This paper is organized as follows:

The main parameters of analyzed SynRM is introduced in section 2. The application of Schwars-Christoffel (S-C) mapping to calculate the permeances of different parts of SynRMs, and preparing the MEC model is explained in section 3. The conclusions of work are presented in section 4.

Fig. 1

2. Introducing the analyzed SynRM

Fig. 1 shows the analyzed SynRM, which has 3 and 4 flux barriers per pole in the rotor, and three-phase double-layer stator winding including corded coils up to 2 slot pitches. The stator phases are illustrated with different colors in Fig. 1. The main parameters of studied SynRM are shown in Table 1.

Table 1

3. MEC model

3.1. An overview

MEC model was firstly introduced by Stovic for modeling and analysis the electric machines while considering the magnetic saturation [14]. The MEC model has been used for electromagnetic analysis of different electric machines [15-16] under steady state and transient conditions. The main property of MEC model is the low computing time and its high accuracy to consider the magnetic saturation in iron parts. The MEC model is also helpful for design optimization which the repetitive computations must be done quickly. In the MEC model, the flux paths and the current-carrying coils are replaced with the permeance elements and the MMF sources, respectively. After developing the MEC model, it can be solved by applying Kirchhoff's Law to the magnetic network.

3.2. Schwartz-Christoffel (S-C) mapping

In this paper, the main idea for permeance calculation is to transform the geometry of relevant part of SynRM into the canonical rectangle by using the S-C mapping, because the permeances of geometry in physical and canonical domains are the same (Conformal maps preserve the premeance). The S-C mapping is a conformal map which can be used to transform a polygon in physical domain to the interior of simple geometry such as upper or lower half-plane, rectangle, disk, and bi-infinite strip in canonical domain [17-20]. To transform the polygon in z-plane (physical domain) having n vertices $z_1,\ldots,z_n$ and interior angles $\alpha_1\pi,\ldots,\alpha_n\pi$ in counterclockwise order into one canonical geometry in w-plane, the formula of S-C mapping is defined as follows:

$$z = f\left(w\right) = A_0 + C_0 \int_{w_0}^{w} \prod_{k=1}^{n-1} \left(w - w_k\right)^{\alpha_k - 1} dw \tag{1}$$

where A_0 and C_0 are the complex constants, $z_k = f\left(w_k\right)$ for $k = 1,\ldots,\left(n-1\right)$, $z = x + jy$ and $w = u + jv$ are the complex numbers in z-plane and w-plane.

For geometries with more than three vertices, the S-C Toolbox [17] should be used to solve the S-C integral (1) to determine the pre-vertices w_k in canonical domain. The S-C Toolbox provides a library of command-line functions. A simple example is used to familiarize the users with these command-line functions. To this end, the following steps should be performed:

1) The S-C Toolbox is available over the Web at

`http://www.math.udel.edu/~driscoll/SC`

2) A simple polygon is created in z-plane by using the following command-line function

```
p=polygon([i -1+i -1-i 1-i 1 0])
```

3) The polygon ‘p’ in z-plane is mapped into one rectangle in w-plane by using the following command-line function

```
alpha=ones(1,6);   alpha(1)=0.5;   alpha(2)=0.5;   alpha(4)=0.5;
alpha(5)=0.5;
g=crrectmap(p,alpha)
```

The array “alpha” shows the values of α_k in Equation (1). In real, “alpha” specifies which vertices of “p” in z-plane should be mapped on the four corners of canonical rectangle in w-plane.

4) The following command-line function is used to evaluate the rectangle in w-plane

```
w=evalinv(g,p)
```

Fig. 2 shows the polygon ‘p’ and rectangle ‘w’ in z-plane and w-plane, respectively.

Fig. 2

Fig. 3

3.3. Rotor permeances

For the analyzed SynRM with 4 flux barriers per pole, the proposed permeance network of rotor is shown in Fig. 3 without considering the end effects. The permeances shown in Fig. 3 are calculated in the following. Fig. 4 shows the geometry of relevant parts of rotor to calculate the permeances P_1- P_3.

Fig. 4

The command-line function `evalinv` is used to evaluate the inverse mapping from polygon “p” to the canonical rectangle “w”. In the case of polygon “p” shown in Fig. 4a, the result of inverse mapping is displayed in Fig. 4b. As shown in Fig. 4a-b, the vertices number 1, 17, 19, and 35 has been mapped on the corners of rectangle in w-plane. Permeance P_1 between sides $p_{1\text{-}17}$ and $p_{19\text{-}35}$ is then calculated as follows:

$$\begin{cases} P_1 = \dfrac{\mu_0 \times \mu_r(B) \times \Delta x \times L}{\Delta y} = 0.162 \times \mu_r(B) \quad (H) \\ \Delta x = real\left(w(17)\right) - real\left(w(1)\right) \\ \Delta y = imag\left(w(19)\right) - imag\left(w(17)\right) \end{cases} \tag{2}$$

where μ_o is the magnetic permeability of air, $\mu_r(B)$ is the non-linear relative permeability of geometry in relevant path in terms of magnetic flux density (B), and L is the axial length.
The geometries with the permeances P_2 and P_3 are shown in Figs. 4c-f. Some permeances such as P_4, P_7, P_{10} and P_{13} are including the permeance of one barrier and the iron part. In a similar way, the permeances P_2- P_{16} are calculated by using the S-C mapping, and the results are presented in Relations (3).

$$\begin{cases} P_2 = 1.06 \times \mu_r(B) \quad (\mu H) \\ P_3 = 0.898 \times \mu_r(B) \quad (\mu H) \\ P_4 = \dfrac{\mu_r(B)}{2.79 + 286875.7 \times \mu_r(B)} \quad (\mu H) \\ P_5 = 0.397 \times \mu_r(B) \quad (\mu H) \\ P_6 = 0.523 \times \mu_r(B) \quad (\mu H) \\ P_7 = \dfrac{\mu_r(B)}{0.419 + 315405.47 \times \mu_r(B)} \quad (\mu H) \\ P_8 = 1.98 \times \mu_r(B) \quad (\mu H) \\ P_9 = 4.73 \times 10^{-8} \times \mu_r(B) \quad (\mu H) \\ P_{10} = \dfrac{\mu_r(B)}{3.17 + 319211.16 \times \mu_r(B)} \quad (\mu H) \\ P_{11} = 2.52 \times \mu_r(B) \quad (\mu H) \\ P_{12} = 0.056 \times \mu_r(B) \quad (\mu H) \\ P_{13} = \dfrac{\mu_r(B)}{1.77 + 245591.8 \times \mu_r(B)} \quad (\mu H) \\ P_{14} = 0.0396 \times \mu_r(B) \quad (\mu H) \\ P_{15} = 0.53 \times \mu_r(B) \quad (\mu H) \\ P_{16} = 0.66 \times \mu_r(B) \quad (\mu H) \end{cases} \tag{3}$$

3.4. Stator and Air-gap permeances

To calculate the air-gap permeances, the outer surface of rotor should be segmented while considering the input/output flux tubes into/from the rotor, as shown in Fig. 5 with red color. Some of air-gap permeances have been displayed in Fig. 5, which shows the permeance between one stator tooth and the specified sides on the rotor surface. To calculate the air-gap permeance between one stator tooth and the edge of rotor surface between vertices "1" and "2" (G_1), the logarithmic conformal map $(z = \log(s))$ is used to transform the air-gap polygon in s-plane (Fig. 6a) into the corresponding geometry in z-plane (Fig. 6b). The S-C mapping (1) is then used to transform the air-gap polygon in z-plane into the canonical rectangle in w-plane, so that the vertices "1", "2", and both ends of relevant tooth-shoe are mapped on the four corners of rectangle. In w-plane (Fig. 6c), the air-gap permeance G_1 is calculated as follows:

$$G_1 = \frac{\mu_0 \times \Delta x \times L}{\Delta y} \tag{4}$$

Fig. 5

In a similar way, some of air-gap permeances (G_1, G_2, G_3, G_4, and G_5 in Fig. 5) are calculated for different rotor positions, and the results in terms of the rotor position (θ_r) are shown in Fig. 7. As shown in Fig. 6, the geometry of stator slots is considered in the air-gap permeance calculation, accurately. The polygon of one stator tooth in z-plane and the corresponding geometry in w-plane which has been obtained by using the S-C mapping are shown in Fig. 8. The value or formula of permeance of one stator tooth (P_{st}), one slot opening (P_{so}), and one segment of stator yoke (P_{sb}) are presented in Relations (5).

Fig. 6

Fig. 7

Fig. 8

$$\begin{cases} P_{st} = 5.1 \times \mu_r(B) \quad (\mu H) \\ P_{so} = 0.0625 \quad (\mu H) \\ P_{sb} = 0.997 \times \mu_r(B) \quad (\mu H) \end{cases} \tag{5}$$

$$
\begin{cases}
I_A(t) = 45\sqrt{2}\,sin\left(100\pi \times t + \left(65 \times \frac{\pi}{180}\right)\right) \\
I_B(t) = 45\sqrt{2}\,sin\left(100\pi \times t + \left(65 \times \frac{\pi}{180}\right) - \left(\frac{2\pi}{3}\right)\right) \\
I_C(t) = 45\sqrt{2}\,sin\left(100\pi \times t + \left(65 \times \frac{\pi}{180}\right) + \left(\frac{2\pi}{3}\right)\right)
\end{cases}
\tag{6}
$$

3.5. Equation system of MEC model

In this paper, three-phase currents (6) are injected into the stator windings when rotating the rotor at synchronous speed 1500 (rpm) and the initial rotor position shown in Fig. 1a. The winding transforms matrixes [14] are used to calculate the magneto motive force (MMF) sources which are placed in series with tooth permeance (P_{st}) in Fig. 5. The matrix of F_{st} can be calculated in terms of stator currents as follows:

$$
\begin{cases}
[F_{st}]_{36\times 1} = [W_t]_{36\times 3} \times [I_s]_{3\times 1} \\
W_t = \left[M_{tmmf}\right]^{-1} \times M_{sat} \times M_{tc} \times M_{cc}
\end{cases}
\tag{7}
$$

where $[M_{tc}]_{36\times 36}$ is a diagonal matrix with the elements equal to the number of turns in each coil, $[M_{cc}]_{36\times 3}$ relates the coil currents to the phase currents, $[M_{sat}]_{36\times 36}$ connects the MMF of coils to MMF in slots, and $[M_{tmmf}]_{36\times 36}$ relates the MMF in slots to the MMF of teeth. Some of these winding transform matrixes are defined in Relations (8)-(9), and others are explained in full details in [14].

$$
M_{tmmf} = \begin{bmatrix}
1 & 0 & 0 & 0 & \cdots & 0 & -1 \\
-1 & 1 & 0 & 0 & \cdots & 0 & 0 \\
0 & -1 & 1 & 0 & 0 & \cdots & 0 \\
0 & 0 & -1 & 1 & 0 & \cdots & 0 \\
\cdots & \vdots & \cdots & \vdots & \cdots & \vdots & \cdots \\
0 & 0 & \cdots & 0 & -1 & 1 & 0 \\
1 & 1 & 1 & 1 & \cdots & 1 & 1
\end{bmatrix}
\tag{8}
$$

$$M_{tc} = 20 \times diag\left(ones\left(1,36\right)\right) \tag{9}$$

As shown in Fig. 9, each column of transfer function $\left[W_t\right]_{36\times3}$ shows the influence of one phase of stator winding on the MMF of stator teeth.

Fig. 9

The nodal magnetic equation in i[th] nodes of stator yoke and stator teeth may be expressed as follows:

$$P_{sb,i} \times \left(U_{sb,i} - U_{sb,i-1}\right) + P_{sb,i+1} \times \left(U_{sb,i} - U_{sb,i+1}\right) + P_{st,i} \times \left(U_{sb,i} - U_{st,i} - F_{st,i}\right) = 0 \tag{10}$$

$$\begin{aligned} &P_{st,i} \times \left(U_{st,i} - U_{sb,i} + F_{st,i}\right) + P_{so} \times \left(U_{st,i} - U_{st,i-1}\right) + P_{so} \times \left(U_{st,i} - U_{st,i+1}\right) \\ &+ \sum_{j=1}^{60} G_{i,j}\left(\theta_r\right) \times \left(U_{st,i} - U_{r,j}\right) = 0 \end{aligned} \tag{11}$$

The compact matrix form of nodal magnetic equations of stator and rotor can be written as follows:

$$\begin{bmatrix} \left[A_{sb-sb}\right]_{36\times36} & \left[A_{sb-st}\right]_{36\times36} & \left[0\right]_{36\times60} \\ \left[A_{st-sb}\right]_{36\times36} & \left[A_{st-st}\right]_{36\times36} & \left[A_{st-r}\right]_{36\times60} \\ \left[0\right]_{60\times36} & \left[A_{r-st}\right]_{60\times36} & \left[A_{r-r}\right]_{60\times60} \end{bmatrix} \begin{bmatrix} \left[U_{sb}\right]_{36\times1} \\ \left[U_{st}\right]_{36\times1} \\ \left[U_r\right]_{60\times1} \end{bmatrix} = -\begin{bmatrix} \left[A_{sb-si}\right]_{36\times3} \\ \left[A_{st-si}\right]_{36\times3} \\ \left[0\right]_{60\times3} \end{bmatrix} \times \left[I_s\right]_{3\times1} \tag{12}$$

where $\left[A_{sb-sb}\right]_{36\times36}$ is the permeance matrix of segments of stator yoke, $\left[A_{sb-st}\right]_{36\times36}$ is a diagonal matrix of permeance of stator teeth, $\left[A_{st-sb}\right] = \left[A_{sb-st}\right]^t$, $\left[A_{st-r}\right]_{36\times60}$ is the air-gap permeance matrix, $\left[A_{r-st}\right] = \left[A_{st-r}\right]^t$, and $\left[A_{r-r}\right]_{60\times60}$ is the permeance matrix of rotor. $\left[U_{sb}\right]_{36\times1}$, $\left[U_{st}\right]_{36\times1}$, and $\left[U_r\right]_{60\times1}$ are the scalar magnetic potential matrix of nodes in stator yoke, stator teeth, and rotor core, respectively.

Fig. 10

The system of non-linear equations (12) is solved using an iterative technique [21] for every rotor position while considering the silicon steel for stator and rotor cores which has the characteristic of $\mu_r = 2000 \times e^{-0.8B^2}$ for the relative magnetic permeability. The flowchart of solving the equation system (12) in an iterative loop for every operating point is shown in Fig. 10 and can be described as follows:

a) The magnetic permeability $\mu_b{}^{m-1}$ is determined for each branch of MEC model in (m-1)th iteration.

b) All permeances are calculated while considering the magnetic permeabilities $\mu_b{}^{m-1}$.

c) The equation system (12) is developed and solved to determine the scalar magnetic potential in all nodes.

d) The magnetic field intensity is calculated for all branches in MEC model $\left(H_b = \frac{\Delta U}{l}\right)$.

e) The magnetic flux density is calculated for all branches by using the B-H curve of stator and rotor cores (B_b).

f) Calculating the new values $\mu_b{}^m$ by using the results of previous step.

g) Checking the convergence criteria. The convergence criteria ε has been considered equal to 0.001.

Fig. 11

For a typical rotor position, the distribution of scalar magnetic potential on the inner surface of stator and outer surface of rotor obtained through solving the equation system (12) have been shown in Fig. 11. To calculate the air-gap magnetic flux density for a relevant operating point (shown in Fig. 11), the distribution of U_s and U_r should be translated into the equivalent virtual currents on the inner and outer radii of air-gap as follows:

$$\begin{cases} I_{v-s}(i) = U_s(i) - U_s(i+1) \\ I_{v-r}(j) = U_r(j) - U_r(j+1) \end{cases} \tag{13}$$

$$T = \frac{2}{R_s + R_r} \tag{14}$$

where $U_s(i)$ and $U_r(j)$ are respectively the scalar magnetic potential in ith node on the inner surface of stator and jth node on the outer surface of rotor. The distribution of equivalent virtual currents corresponding to the operating point in Fig. 11 is illustrated in Fig. 12.

Fig. 12

The equivalent virtual currents shown in Fig. 12 represent the MMF drops due to stator slots, the flux barriers of rotor, and the magnetic saturation in iron parts. Therefore, the motor geometry is replaced with one annular domain including the equivalent virtual currents (physical domain in Fig. 13). The conformal map (14) is used to transform the physical slotless air-gap into the canonical slotless air-gap in Fig. 13, which has the average radius of one meter $(b < 1 < a)$.

Fig. 13

Hague's solution [21-22] is used to calculate the radial and tangential components of air-gap flux density due to the equivalent virtual currents (I_k) in canonical slotless air-gap as follows:

$$B_{r-c}(r,\theta) = -\frac{\mu_0}{r} \times \sum_{k=1}^{72} \left[\sum_{n=1}^{\infty} n \times \left(A_{n,k} \times r^n - \left(\frac{I_k \times r_k{}^n}{2n\pi} + B_{n,k} \right) \times r^{-n} \right) sin(n \times \Delta\theta_k) \right] \quad (15)$$

$$B_{t-c}(r,\theta) = -\frac{\mu_0}{r} \times \sum_{k=1}^{72} \left[\frac{I_k}{2\pi} + \sum_{n=1}^{\infty} n \times \left(A_{n,k} \times r^n + \left(\frac{I_k \times r_k{}^n}{2n\pi} + B_{n,k} \right) \times r^{-n} \right) cos(n \times \Delta\theta_k) \right] \quad (16)$$

$$\begin{cases} A_{n,k} = \dfrac{-I_k(\mu_1 - \mu_2)\left[b^{2n}(\mu_3 - \mu_2) + r_k{}^{2n}(\mu_3 + \mu_2) \right]}{r_k{}^n \times (2n\pi) \times \left[b^{2n}(\mu_2 - \mu_3)(\mu_1 - \mu_2) + a^{2n}(\mu_2 + \mu_3)(\mu_1 + \mu_2) \right]} \\ B_{n,k} = \dfrac{b^{2n} \times I_k(\mu_3 - \mu_2)\left[a^{2n}(\mu_1 + \mu_2) + r_k{}^{2n}(\mu_1 - \mu_2) \right]}{r_k{}^n \times (2n\pi) \times \left[b^{2n}(\mu_2 - \mu_3)(\mu_1 - \mu_2) + a^{2n}(\mu_2 + \mu_3)(\mu_1 + \mu_2) \right]} \\ \Delta\theta_k = \theta - \theta_k \end{cases} \quad (17)$$

$$\begin{cases} B_r(r,\theta) = T \times B_{r-c}(r,\theta) \\ B_t(r,\theta) = T \times B_{t-c}(r,\theta) \end{cases} \quad (18)$$

where r_k and θ_k are respectively the radial and angular positions of virtual current I_k. μ_1, μ_2, and μ_3 are the magnetic permeability of stator core, air-gap, and rotor core in canonical domain. The formula (18) is then used to calculate the components of air-gap flux density in physical domain.

Fig. 14

In [23], one approximate analytical model based on the inverse air-gap function was used to calculate the air-gap flux density distribution in the permanent magnet synchronous machines. For relevant operating point mentioned in Figs. 11-12 and by using Hague's solution, the components of air-gap flux density obtained through MEC model and FEM are shown and compared in Fig. 14. The electromagnetic torque of analyzed SynRM can be calculated as follows:

$$T_e(\theta_r)=\sum_{i=1}^{36}\sum_{j=1}^{60}\left(\left[U_s(i)-U_r(j)\right]^2\times\frac{dG(i,j)}{d\theta_r}\right) \quad (19)$$

where θ_r is the rotor position, and $G(i,j)$ is the air-gap permeance between ith tooth of stator and jth node of rotor.

As shown in Fig. 1b, the analyzed SynRM has been also designed with 3 flux barrier per pole in rotor. The results of eletromagnetic torque obtained through MEC model and FEM are shown in Fig. 15 while considering two topologies of rotor with 3 and 4 flux barriers per pole. As shown, there is a good agreement between corresponding results.

Fig. 15

For both topologies of analyzed SynRM, the average and peak-peak values of electromagnetic torque are presented in Table 2 while considering I_{RMS}=45 (A). As shown, torque ripple is about 13.7 percent for both topologies which is due to the stator slots, flux barriers, magnetic saturation, and the distribution of stator windings. The effect of step skew of rotor in SynRMs has been studied in [24]. Generally, it can be said the average torque and the torque ripple are reduced due to the rotor skewing of SynRMs, simultaneously.

Table 2

Fig. 16

Table 3

For an operating point under the over-load condition, which the RMS value of stator phase current is 90 (A), the electromagnetic torques of analyzed SynRM with 4 flux barriers per pole obtained through proposed MEC model and FEM are illustrated and verified in Fig. 15c. For two analyzed operating points of this topology, the average and peak-peak values of T_e are shown in Table 3. As shown in Table 3, despite doubling the stator phase current, the average value of T_e and torque ripple have been respectively increased about 70 and 168 percent due to the nonlinearity effets of magnetic saturation. Fig. 16 shows the key parameters of flux barriers. It should be noted that the variables r_b and α_b are interdependent due to the hyperbolic structure of the flux barriers. By using the proposed MEC model, the sensitivity of produced electromagnetic torque of the analyzed SynRM (with 4 flux barriers per pole) to the main parameters of flux barriers are illustrated in Fig. 17.

Fig. 17

Fig. 18

Fig. 19

Fig. 20

The observed differences in the results shown in Figs. 14-15 are due to the negligible error in magnetic saturation modeling in the rotor ribs. For example, the relative magnetic permeability (μ_r) in one rotor rib obtained through MEC and FE models are shown and compared in Fig. 18.

A prototype of analyzed SynRM with 4 flux barriers per pole has been manufactured and tested with V/f drive and under no-load condition. The pictures of manufactured SynRM, test rig, and experiment results are shown in Fig. 19. The phase currents of analyzed SynRM obtained through proposed MEC model and FEM are shown and compared in Fig. 20 when applying a three-phase voltage source with the RMS value of 380.3 (V) and the frequency of 50 (Hz) under the no-load condition. As shown in Fig. 20, the RMS value of stator phase current is in agreement with the experiment result.

4. Conclusion

A new MEC model was presented in this paper, which is including a limited number of permeances for accurate and fast modeling the SynRMs. The calculation of an operating point in MEC and FE models takes about 0.1 (s) and 5 (s), respectively. The S-C map was used to calculate the permeance of different parts of rotor core and barriers which have the complex geometries. To calculate the air-gap permeances, a logarithmic conformal map was firstly used to transform the physical slotted air-gap into an air-gap polygon in z-plane, which the condition has prepared to apply the S-C map. In this way, all permeances have been calculated, accurately. Then, the non-linear equation system of MEC model was prepared and solved using an iterative technique for obtaining the distribution of scalar magnetic potential in different parts of the analyzed SynRM. The MMF drops due to the rotor barrier, stator slots, and iron parts are translated into the equivalent vewirtual currents. Hague's solution and a simple conformal map were then used to calculate the components of air-gap flux density while considering all non-ideal effects. In final, the electromagnetic torque and phase current of analyzed SynRM was calculated and analyzed by using the proposed MEC model, FEM and the experiment set-up. As was seen, there is a good agreement between corresponding results. It should be noted that the proposed MEC model can be extended and used for analysis of all electric machines.

5. References

[1]. Babetto, C., Bacco, G., and Bianchi, N., “Synchronous reluctance machine optimization for high speed applications”, *IEEE Trans. Energy Convers.*, **33**(3), pp. 1266-1273, (2018). **DOI:** 10.1109/TEC.2018.2800536

[2]. Mukherjee, V., Rasilo, P., Martin, F., and et al., "Analysis of electromagnetic force ripple in a bearingless synchronous reluctance motor", *IEEE Trans. Magn.*, **57**(2), Article Sequence Number: 8103908, (2021). **DOI:** 10.1109/TMAG.2020.3041703

[3]. Tawfiq, K. B., Ibrahim, M. N., EL-Kholy, E. E., and et al., “Performance analysis of a rewound multiphase synchronous reluctance machine”, *IEEE J. Emerg. Sel. Topics Power Electron.*, **10**(1), pp. 297-309, (2022). **DOI:** 10.1109/JESTPE.2021.3106591

[4]. Farhadian, M., Moallem, M., and Fahimi, B., “Multimodal optimization algorithm for torque ripple reduction in synchronous reluctance motors”, *IEEE Access*, **10**, pp. 26628-26636, (2022). **DOI:** 10.1109/ACCESS.2022.3155158

[5]. Maroufian, S. S., and Pillay, P., “Torque characterization of a synchronous reluctance machine using an analytical model”, *IEEE Trans. Transport. Electrific.*, **4**(2), pp. 506-516, (2018). **DOI:** 10.1109/TTE.2018.2794828

[6]. Naseer, M. U., Kallaste, A., Asad, B., and et al., "Modified winding function analysis of synchronous reluctance motor for design iteration purposes", *IEEE Trans. Magn.*, **58**(9), Article Sequence Number: 7500704, (2022). **DOI:** 10.1109/TMAG.2022.3164189

[7]. Ahmed, F., Martin, F., Das, N., and et al., "Analytical modeling of a six-phase bearingless synchronous reluctance machine using winding function theory", *IEEE Energy Conversion Congress and Exposition (ECCE)*, USA, (2023). **DOI:** 10.1109/ECCE53617.2023.10361945

[8]. Tessarolo, A., "Modeling and analysis of synchronous reluctance machines with circular flux barriers through conformal mapping", *IEEE Trans. Magn.*, **51**(4), Article Sequence Number: 8104411, (2015). **DOI:** 10.1109/TMAG.2014.2363434

[9]. Yan, D., Xia, C., Guo, L., and et al**, "**Design and analysis for torque ripple reduction in synchronous reluctance machine**",** *IEEE Trans. Magn.*, **54**(11), Article Sequence Number: 8203605, (2018). **DOI:** 10.1109/TMAG.2018.2847735

[10]. Murataliyev, M., Degano, M., and Galea, M., "A novel sizing approach for synchronous reluctance machines", *IEEE Trans. Ind. Electron.*, **68**(3), pp. 2083-2095, (2021). **DOI:** 10.1109/TIE.2020.2975461

[11]. Bianchi, N., Bolognani, S., Bon, D., and et al., “Torque harmonic compensation in a synchronous reluctance motor”, *IEEE Trans. Energy Convers.*, **23**(2), pp. 466-473, (2008). **DOI:** 10.1109/TEC.2007.914357

[12]. Bacco, G., Bianchi, N., and Mahmoud, H., “A nonlinear analytical model for the rapid prediction of the torque of synchronous reluctance machines”, *IEEE Trans. Energy Convers.*, **33**(3), pp. 1539-1546, (2018). **DOI:** 10.1109/TEC.2018.2808168

[13]. Mahmoud, H., Bianchi, N., Bacco, G., and et al., "Nonlinear analytical computation of the magnetic field in reluctance synchronous machines", *IEEE Trans. Ind. Appl.*, **53**(6), pp. 5373–5382, (2017). **DOI:** 10.1109/TIA.2017.2746560

[14]. Stovic, V., "Dynamics of saturated electric machines", Springer-Verlag New York Inc, (1989). **DOI:** 10.1007/978-1-4613-8933-0

[15]. Hemeida, A., Billah, M. M., Kudelina, K., and et al., "Magnetic equivalent circuit and Lagrange interpolation function modeling of induction machines under broken bar faults", *IEEE Trans. Magn.*, **60**(3), Article Sequence Number: 8200704, (2024). **DOI:** 10.1109/TMAG.2023.3306207

[16]. Korman, O., Nardo, M. D., Riccio, J., and et al., "Distributed magnetic equivalent circuit modeling of synchronous machines", *IEEE Trans. Ind. Appl.*, **61**(1), pp. 4–15, (2015). **DOI:** 10.1109/TIA.2024.3462898

[17]. Driscoll, T. A., and Trefethen, L. N., "Schwarz-Christoffel mapping", Cambridge University Press, (2002). **DOI:** 10.1017/CBO9780511546808

[18]. Rezaee-Alam, F., Hamidi, A., and Hosseini, M., "A new hybrid analytical model based on winding function theory for analysis of unbalanced two-phase induction motors", *Scientia Iranica*, **31**(2), pp. 149-160, (2024). **DOI:** 10.24200/sci.2022.57654.5348

[19]. Li, Z., Wu, L., Li, Y., and et al., "Hybrid analytical model of permanent magnet linear motor considering iron saturation and end effect", *IEEE Trans. Energy Convers.*, **39**(3), pp. 2008-2017, (2024). **DOI:** 10.1109/TEC.2024.3354488

[20]. Boughrara, K., Ibtiouen, R., Zarko, D., and et al., "Magnetic field analysis of external rotor permanent-magnet synchronous motors using conformal mapping", *IEEE Trans. Magn.*, **46**(9), pp. 3684-3693, (2010). **DOI:** 10.1109/TMAG.2010.2047508

[21]. Rezaee-Alam, F., Nazari Marashi, A., Roozbehani, S., "Modified magnetic equivalent circuit model for magnetic field analysis of one cage-rotor induction motor used in electric submersible pumps", *IET Elec. Power. Appl.*, **17**(6), pp. 802-812, (2023). **DOI:** 10.1049/elp2.12305

[22]. Rezaee-Alam, F., "An Accurate Magnetic Equivalent Circuit Model for Modeling and Analysis of Variable Reluctance Energy Harvesters", *Scientia Iranica*, Articles in Press, (2024). **DOI:** 10.24200/sci.2023.61076.7133

[23]. Babaei, M., Feyzi, M., and Nazari Marashi, A., "Incorporating the coupled effects of slot opening, armature reaction and saturation in the model of the airgap flux density distribution of permanent magnet synchronous machines", *IET Elec. Power. Appl.*, **18**(2), pp. 240-251, (2024). **DOI:** 10.1049/elp2.12384

[24]. Islam, M. S., Shrestha, A., and Islam, M., "Effect of Step Skew in Synchronous Reluctance Machines for High Performance Applications", *IEEE Energy Conversion Congress and Exposition (ECCE)*, (2022). **DOI:** 10.1109/ECCE50734.2022.9947850

Fig. 1. 2D Geometry of analyzed SynRMs, **(a)** 3 flux barriers per pole, **(b)** 4 flux barriers per pole

Fig. 2. Simple illustration of S-C map, **(a)** z-plane, **(b)** w-plane

Fig. 3. Proposed MEC model of rotor

Fig. 4. Calculation of rotor permeances, **(a)** z-plane, **(b)** w-plane, **(c)** z-plane, **(d)** w-plane, **(e)** z-plane, **(f)** w-plane

Fig. 5. A zoomed view of air-gap and stator permeances

Fig. 6. Geometries of air-gap polygon in different domains, **(a)** s-plane, **(b)** z-plane, **(c)** w-plane

Fig. 7. Air-gap permeances

Fig. 8. Geometry of one stator tooth, **(a)** z-plane, **(b)** w-plane

Fig. 9. Winding function of stator phases

Fig. 10. Flowchart of an iterative loop

Fig. 11. Distribution of scalar magnetic potential, **(a)** on the inner surface of stator, **(b)** on the outer surface of rotor

Fig. 12. Distribution of equivalent virtual currents, **(a)** on the inner surface of stator, **(b)** on the outer surface of rotor

Fig. 13. Equivalent slotless air-gaps

Fig. 14. Components of air-gap flux density, **(a)** Radial component, **(b)** Tangential component

Fig. 15. Electromagnetic torque, **(a)** Topology with 3 flux barriers per pole (under I_{RMS}=45 (A)), **(b)** Topology with 4 flux barriers per pole (under I_{RMS}=45 (A)), **(c)** Topology with 4 flux barriers per pole (under I_{RMS}=90 (A))

Fig. 16. Main parameters of flux barriers

Fig. 17. Torque sensitivity to flux barrier geometry**, (a)** Average torque sensitivity to first flux barrier**, (b)** Torque ripple sensitivity to first flux barrier**, (c)** Average torque sensitivity to second flux barrier**, (d)** Torque ripple sensitivity to second flux barrier**, (e)** Average torque sensitivity to third flux barrier**, (f)** Torque ripple sensitivity to third flux barrier**, (g)** Average torque sensitivity to forth flux barrier, **(h)** Torque ripple sensitivity to forth flux barrier

Fig. 18. Comparison of μ_r in one rotor rib

Fig. 19. Experiment set-up and results, **(a)** Manufactured machine, **(b)** Test rig, **(c)** Magnitude of frequency and RMS value of phase current, **(d)** RMS value of line-line voltage

Fig. 20. Stator phase current

Table 1. Main parameters of analyzed SynRM

Table 2. Torque results for two rotor topologies

Table 3. Torque results for different phase currents

.

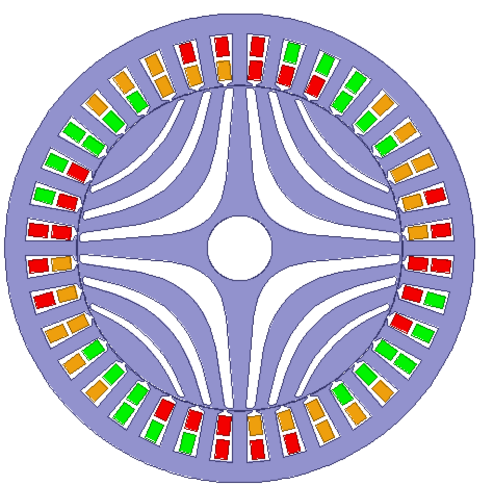

(a)

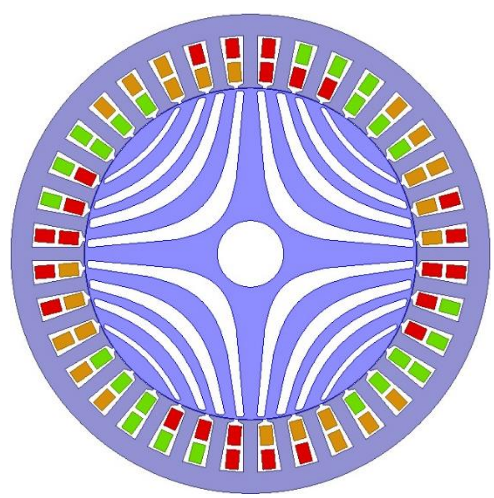

(b)

Fig. 1

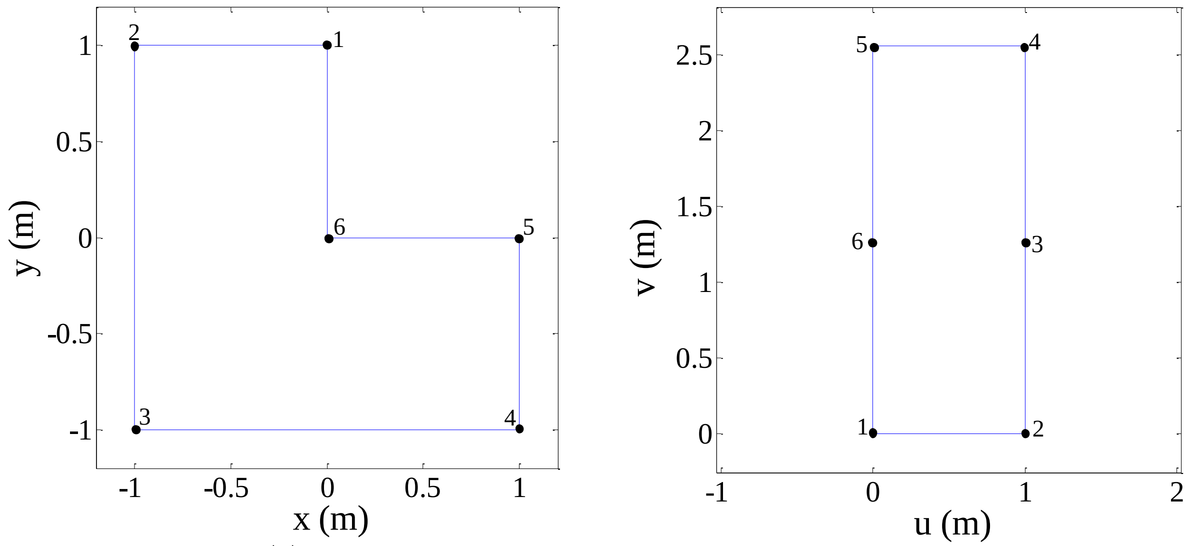

y (m)
x (m)
v (m)
u (m)

(a) **(b)**

Fig. 2

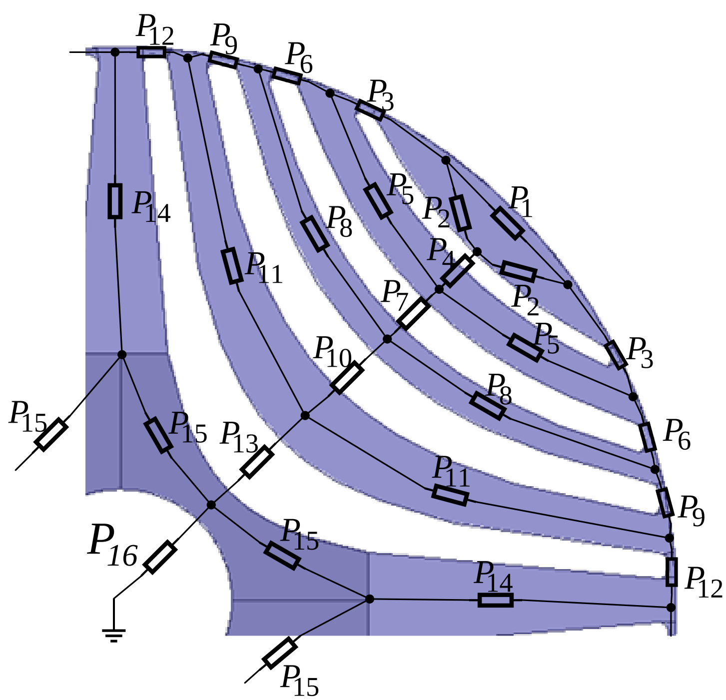

P12
P9
P6
P3
P14
P11
P8
P5
P2
P1
P4
P7
P2
P5
P3
P10
P8
P6
P15
P15
P13
P11
P9
P16
P15
P14
P12
P15

Fig. 3

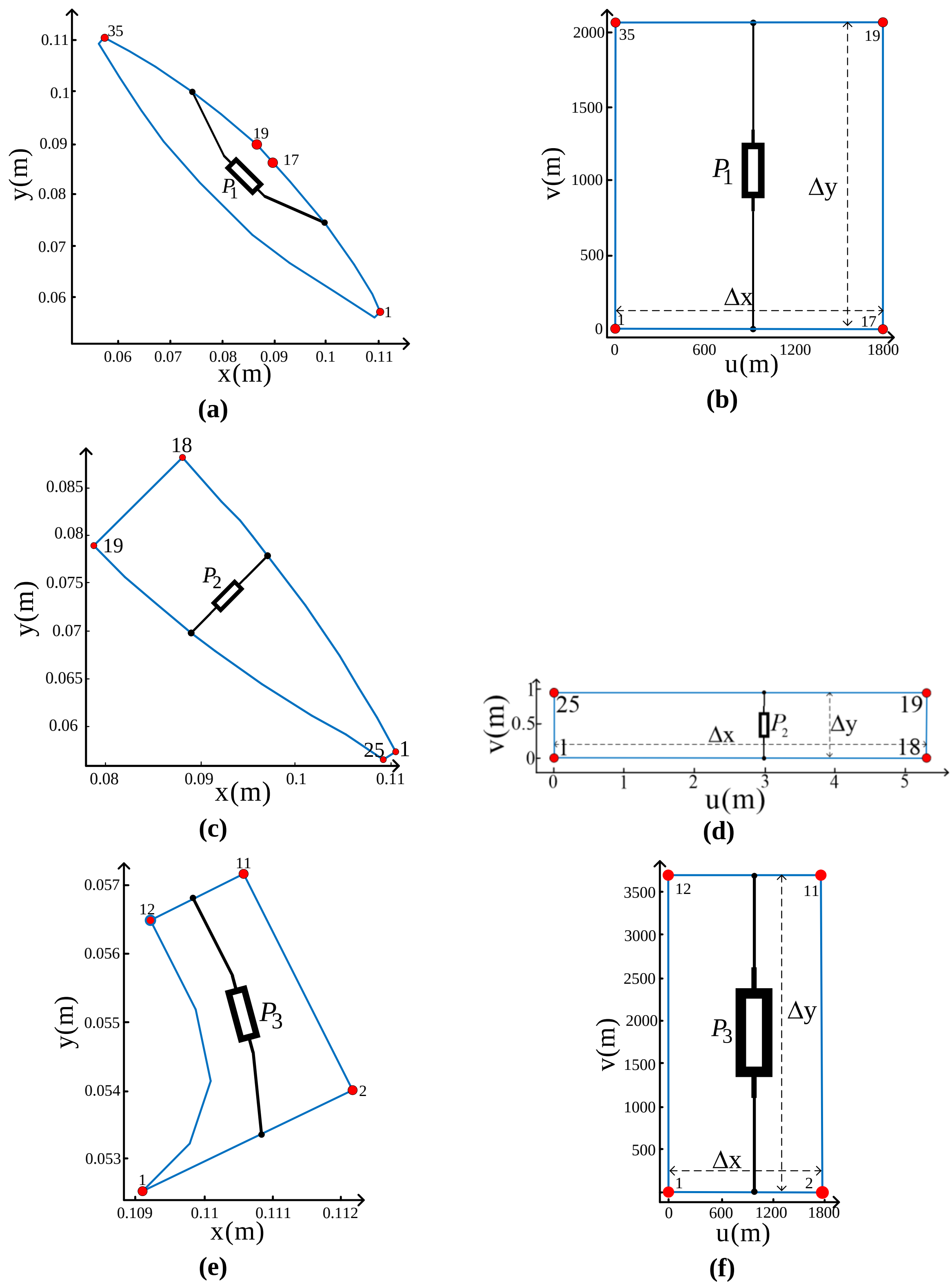
0.11
0.1
0.09
0.08
0.07
0.06
y(m)
35
19
17
1
P1
0.06 0.07 0.08 0.09 0.1 0.11
x(m)
(a)
2000
1500
1000
500
0
v(m)
35
19
P1
Δy
Δx
1
17
0 600 1200 1800
u(m)
(b)
0.085
0.08
0.075
0.07
0.065
0.06
y(m)
18
19
P2
25
1
0.08 0.09 0.1 0.11
x(m)
(c)
1
0.5
0
v(m)
25
19
P2
Δy
Δx
1
18
0 1 2 3 4 5
u(m)
(d)
0.057
0.056
0.055
0.054
0.053
y(m)
11
12
P3
2
1
0.109 0.11 0.111 0.112
x(m)
(e)
3500
3000
2500
2000
1500
1000
500
v(m)
12
11
P3
Δy
Δx
1
2
0 600 1200 1800
u(m)
(f)

Fig. 4

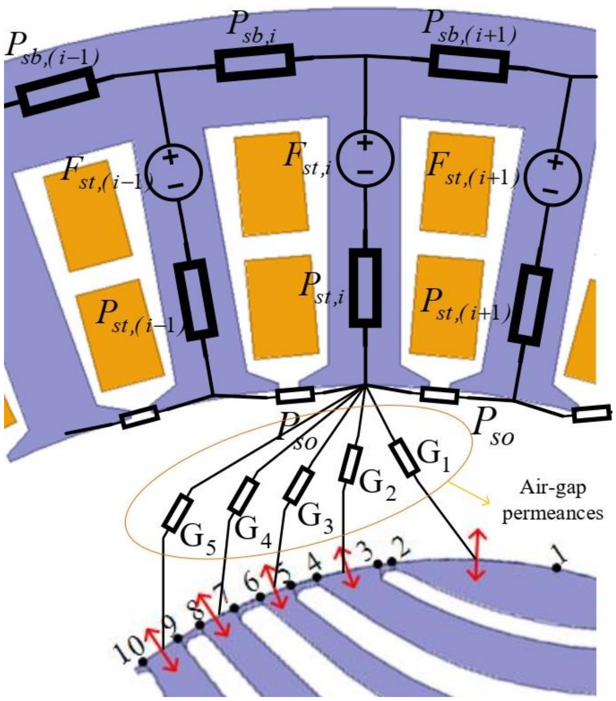

Fig. 5

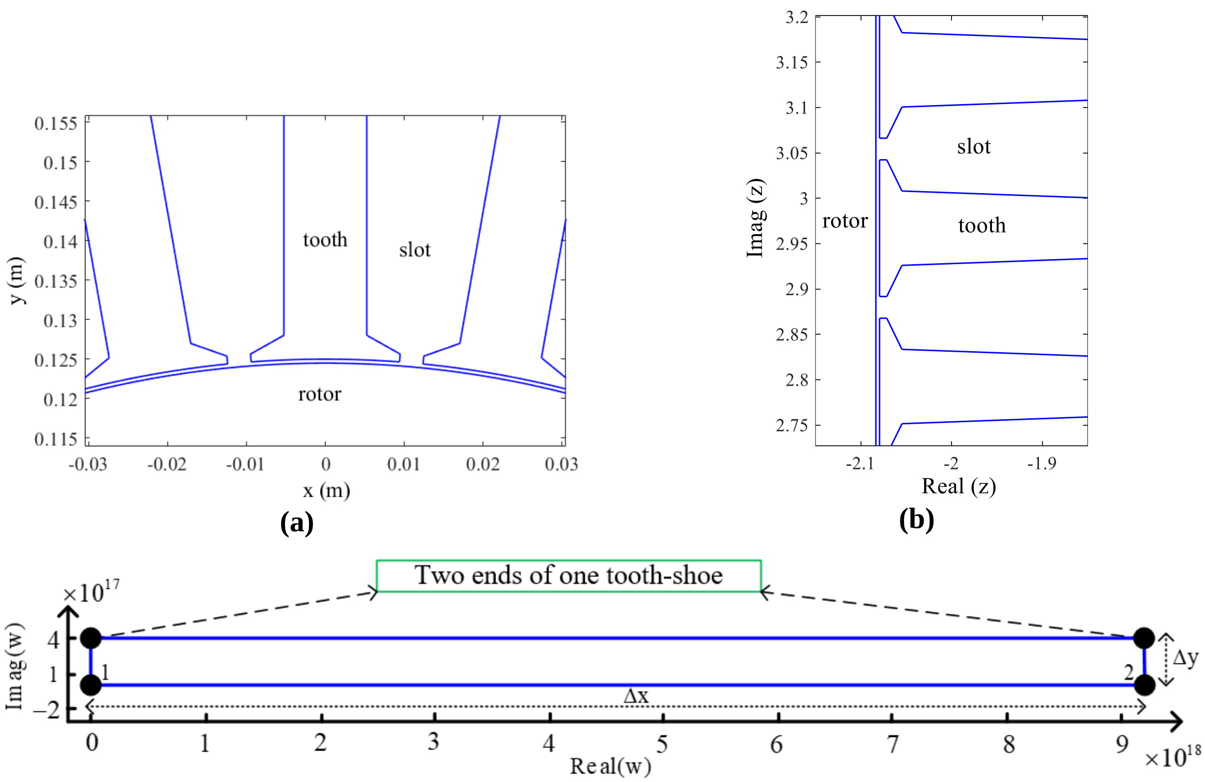

(a) **(b)**

(c)

Fig. 6

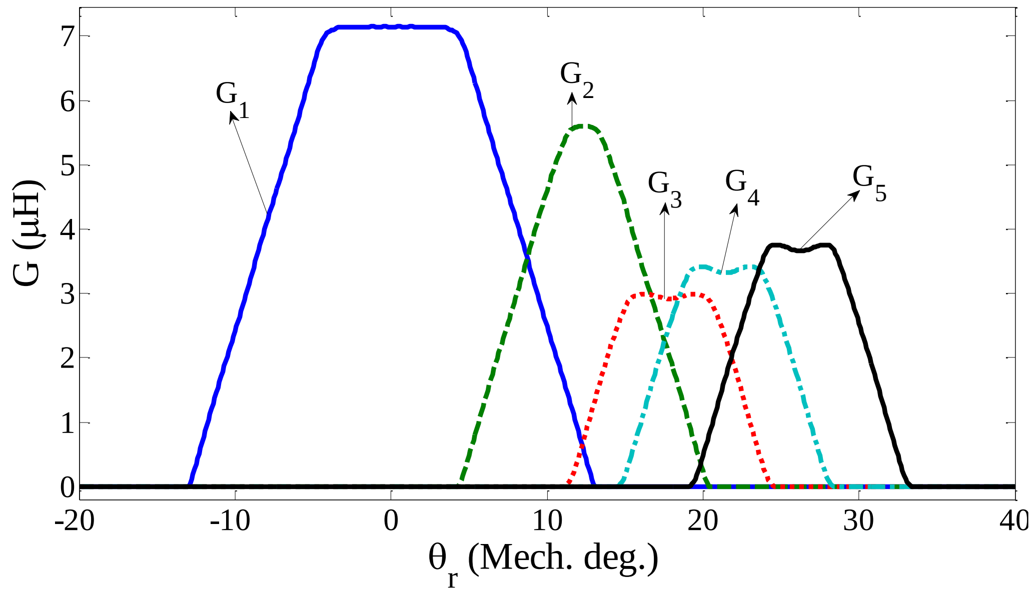

G (μH)
θr (Mech. deg.)
G1
G2
G3
G4
G5

Fig. 7

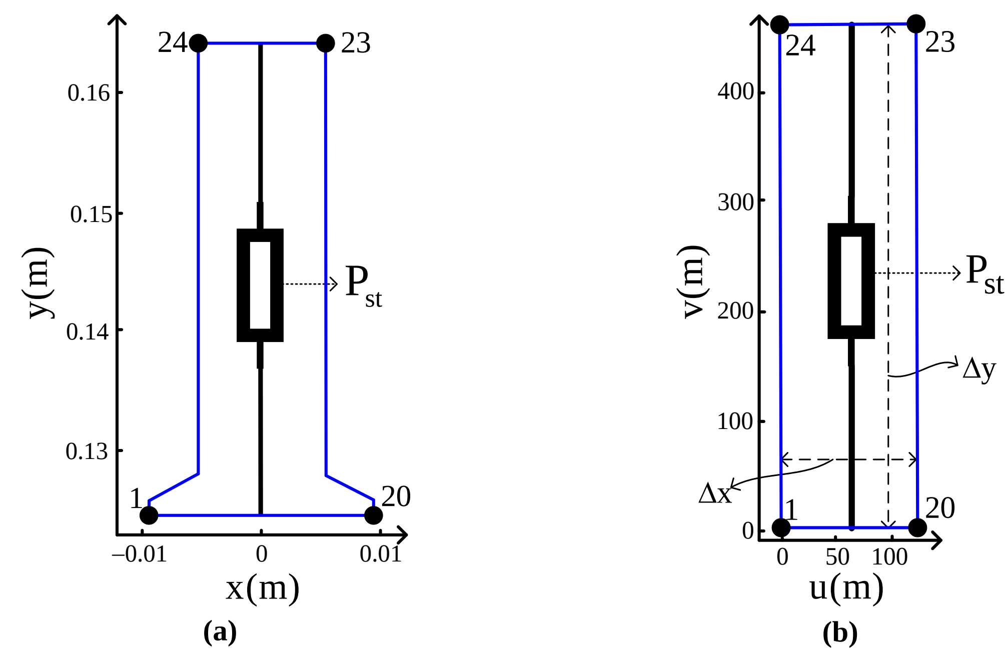

y(m)
x(m)
24
23
1
20
Pst
(a)
v(m)
u(m)
24
23
1
20
Pst
Δy
Δx
(b)

Fig. 8

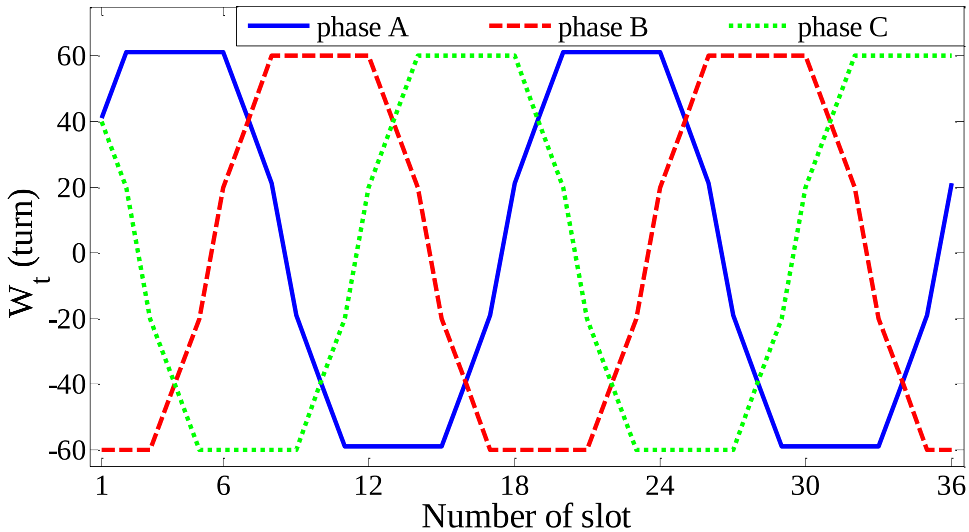

phase A
phase B
phase C
60
40
20
0
-20
-40
-60
W_t (turn)
1
6
12
18
24
30
36
Number of slot

Fig. 9

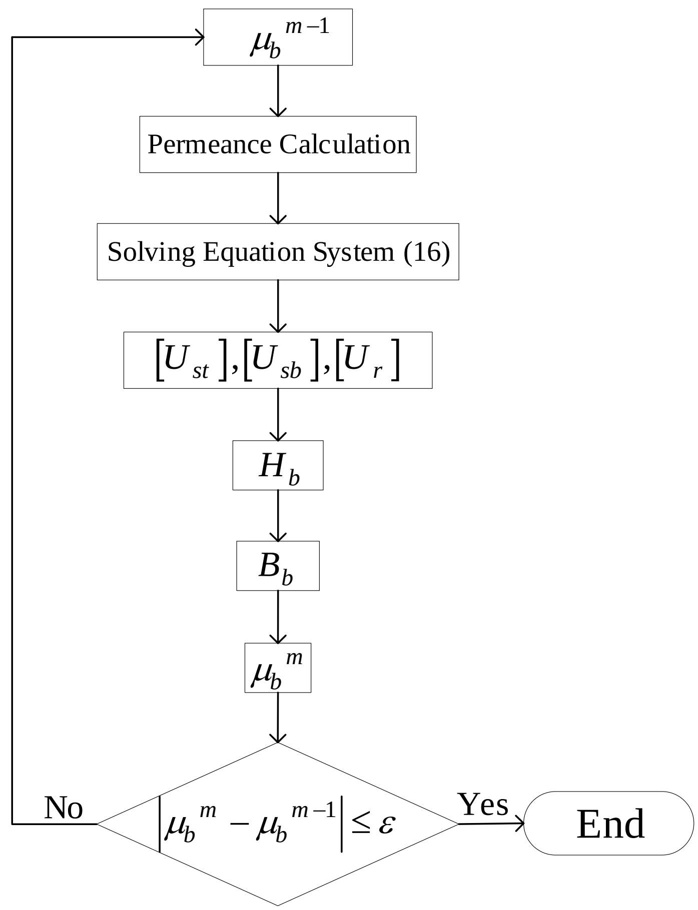
μ_b^{m-1}
Permeance Calculation
Solving Equation System (16)
$[U_{st}],[U_{sb}],[U_r]$
H_b
B_b
μ_b^{m}
$\left|\mu_b^{m}-\mu_b^{m-1}\right| \le \varepsilon$
No
Yes
End

Fig. 10

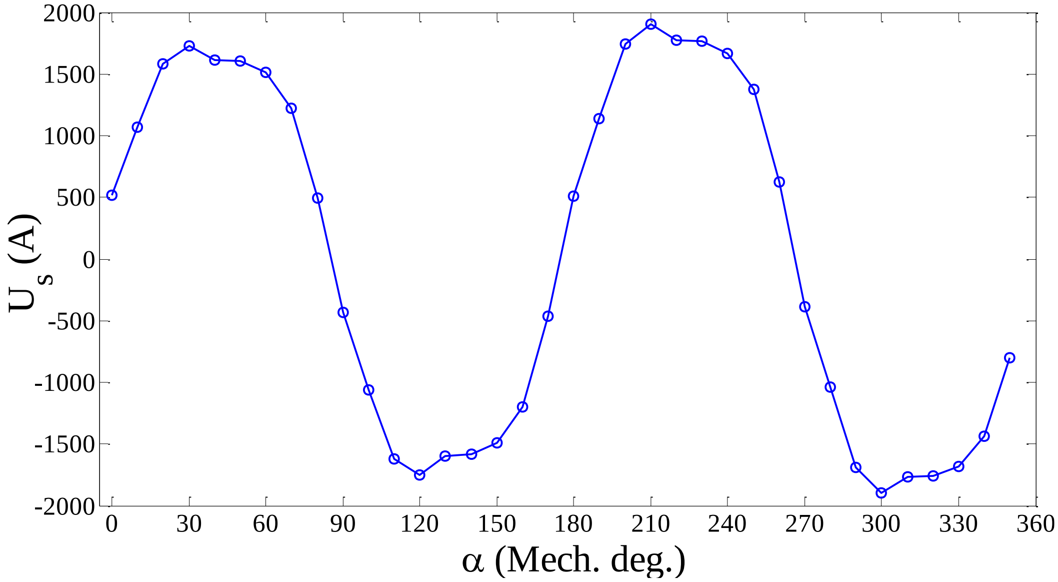
2000
1500
1000
500
0
-500
-1000
-1500
-2000
U_s (A)
0 30 60 90 120 150 180 210 240 270 300 330 360
α (Mech. deg.)

(a)

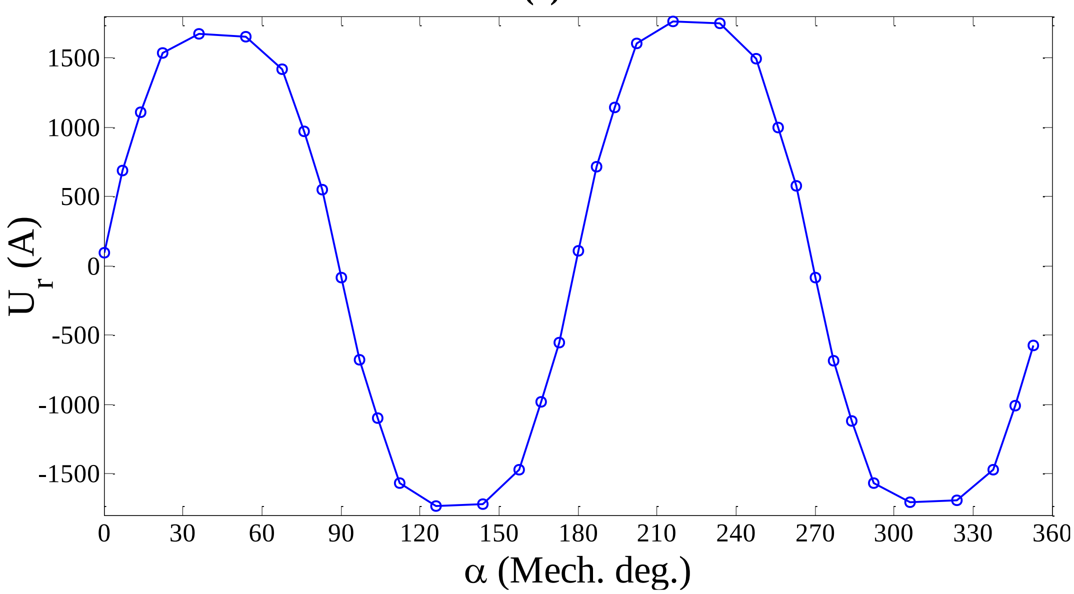
1500
1000
500
0
-500
-1000
-1500
U_r (A)
0 30 60 90 120 150 180 210 240 270 300 330 360
α (Mech. deg.)

(b)

Fig. 11

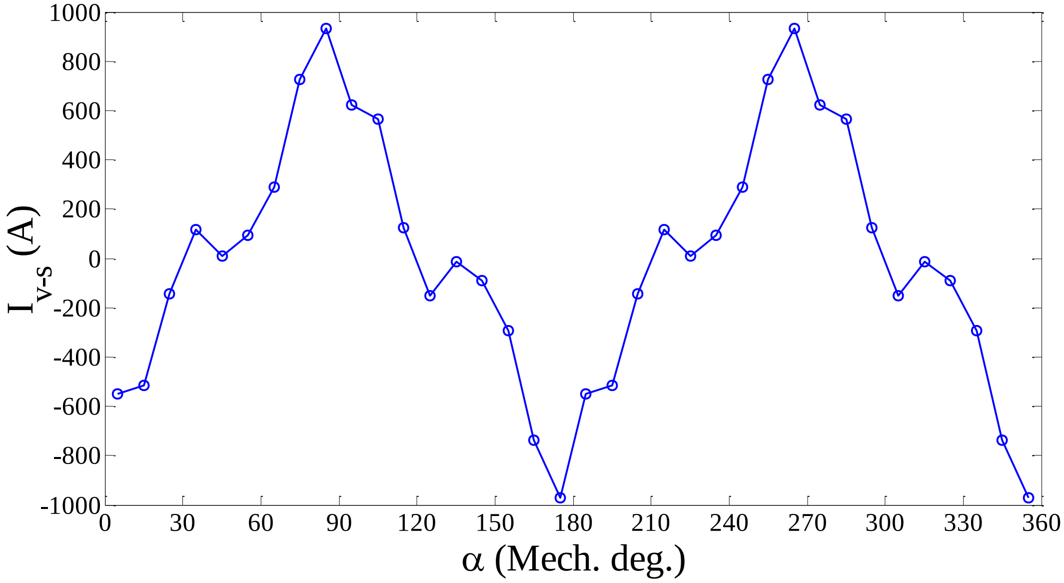
1000
800
600
400
200
0
-200
-400
-600
-800
-1000
I_{v-s} (A)
0 30 60 90 120 150 180 210 240 270 300 330 360
α (Mech. deg.)

(a)

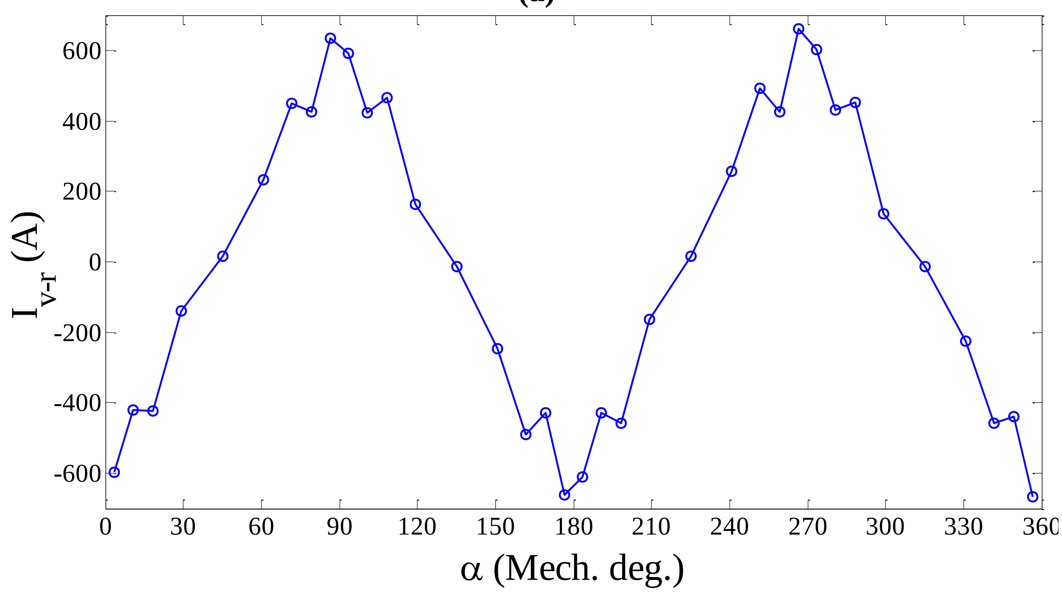
600
400
200
0
-200
-400
-600
I_{v-r} (A)
0 30 60 90 120 150 180 210 240 270 300 330 360
α (Mech. deg.)

(b)

Fig. 12

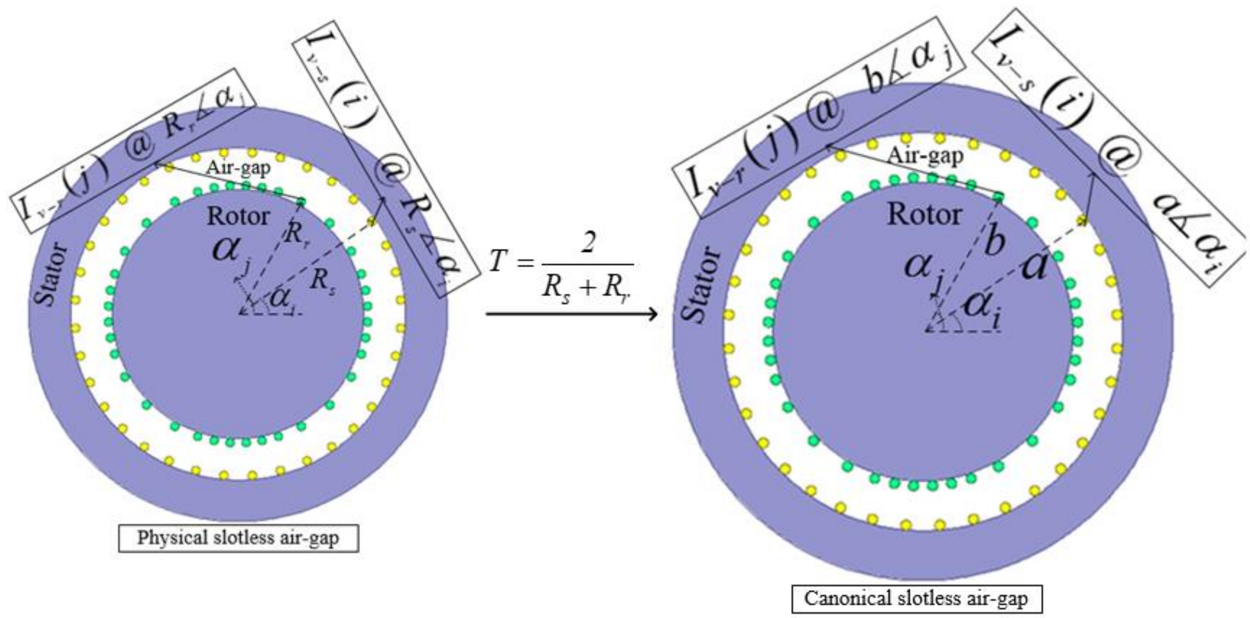
$I_{v-r}(j)$ @ $R_r\angle\alpha_j$
$I_{v-s}(i)$ @ $R_s\angle\alpha_i$
Air-gap
Rotor
Stator
R_r
R_s
α_j
α_i
Physical slotless air-gap
$T=\dfrac{2}{R_s+R_r}$
$I_{v-r}(j)$ @ $b\angle\alpha_j$
$I_{v-s}(i)$ @ $a\angle\alpha_i$
Air-gap
Rotor
Stator
b
a
α_j
α_i
Canonical slotless air-gap

Fig. 13

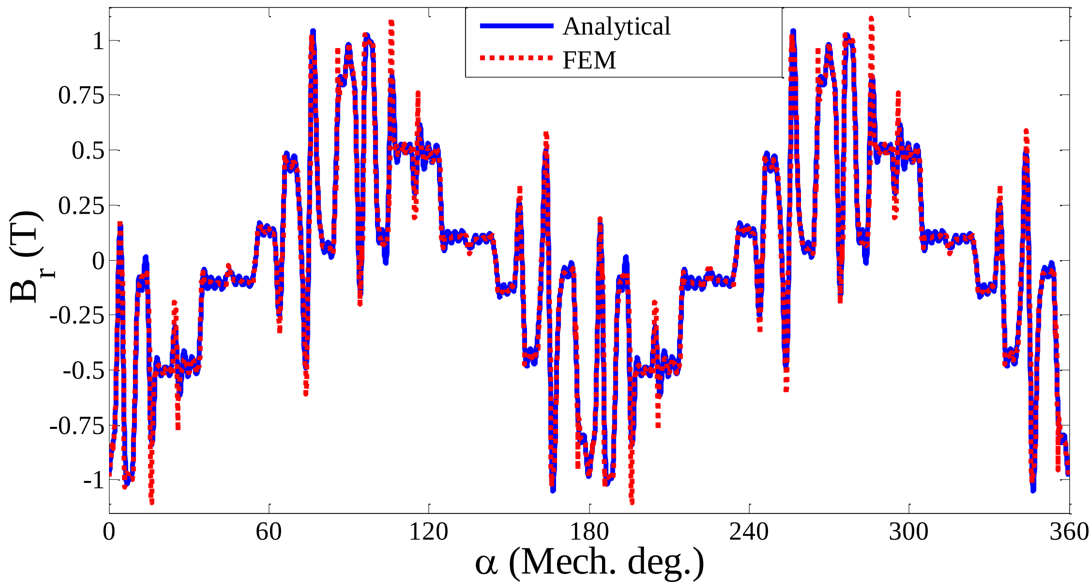

Analytical
FEM
B_r (T)
1
0.75
0.5
0.25
0
-0.25
-0.5
-0.75
-1
0
60
120
180
240
300
360
α (Mech. deg.)

(a)

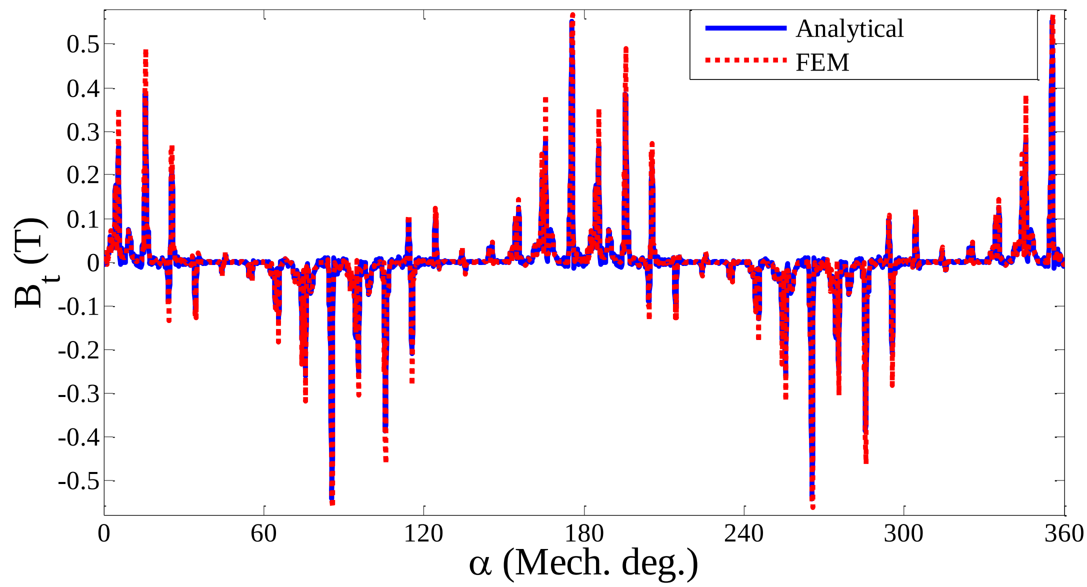

Analytical
FEM
B_t (T)
0.5
0.4
0.3
0.2
0.1
0
-0.1
-0.2
-0.3
-0.4
-0.5
0
60
120
180
240
300
360
α (Mech. deg.)

(b)

Fig. 14

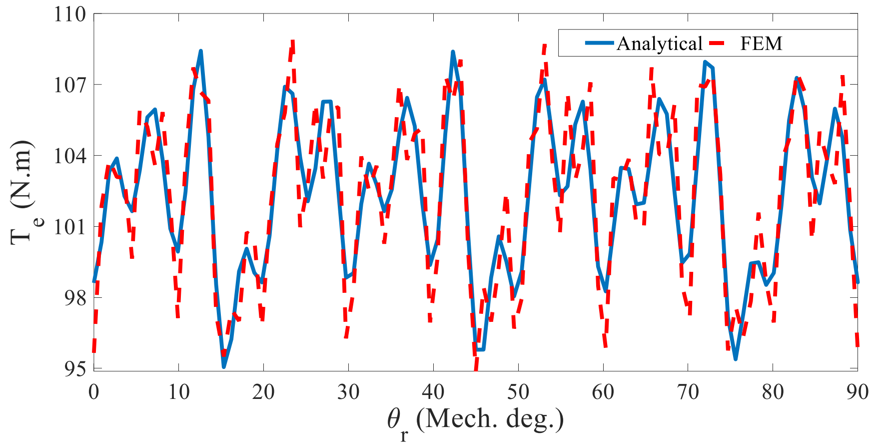

Analytical
FEM
110
107
104
101
98
95
0
10
20
30
40
50
60
70
80
90
T_e (N.m)
θ_r (Mech. deg.)

(a)

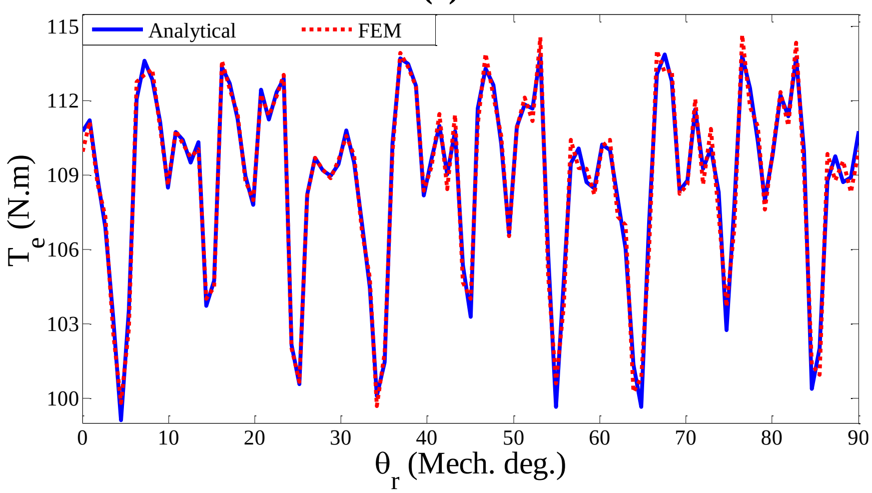

Analytical
FEM
115
112
109
106
103
100
0
10
20
30
40
50
60
70
80
90
T_e (N.m)
θ_r (Mech. deg.)

(b)

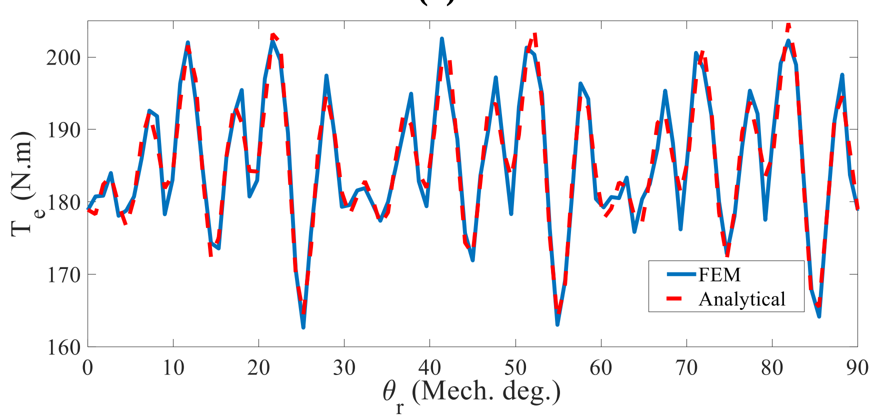

FEM
Analytical
200
190
180
170
160
0
10
20
30
40
50
60
70
80
90
T_e (N.m)
θ_r (Mech. deg.)

(c)

Fig. 15

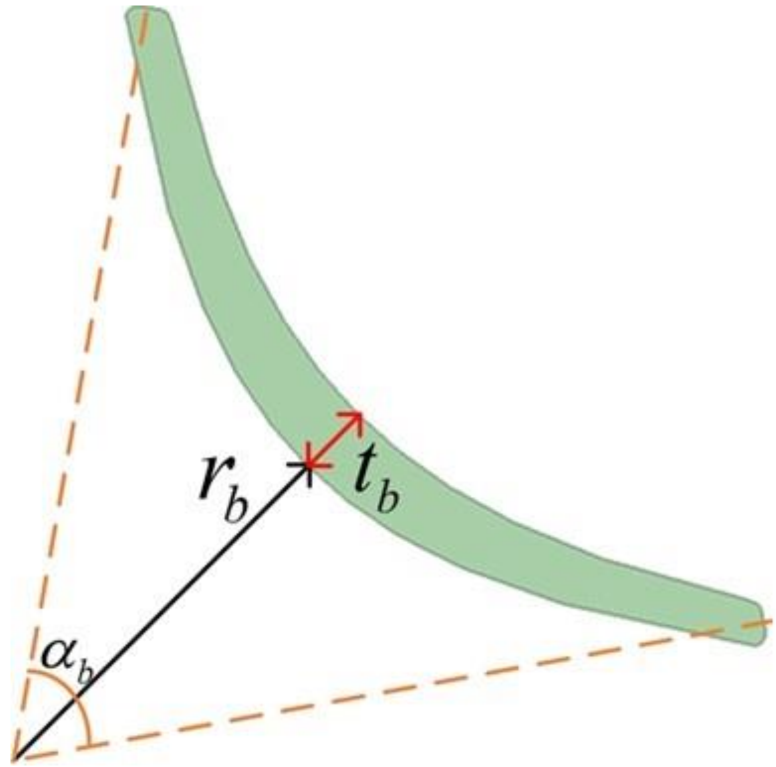

Fig. 16

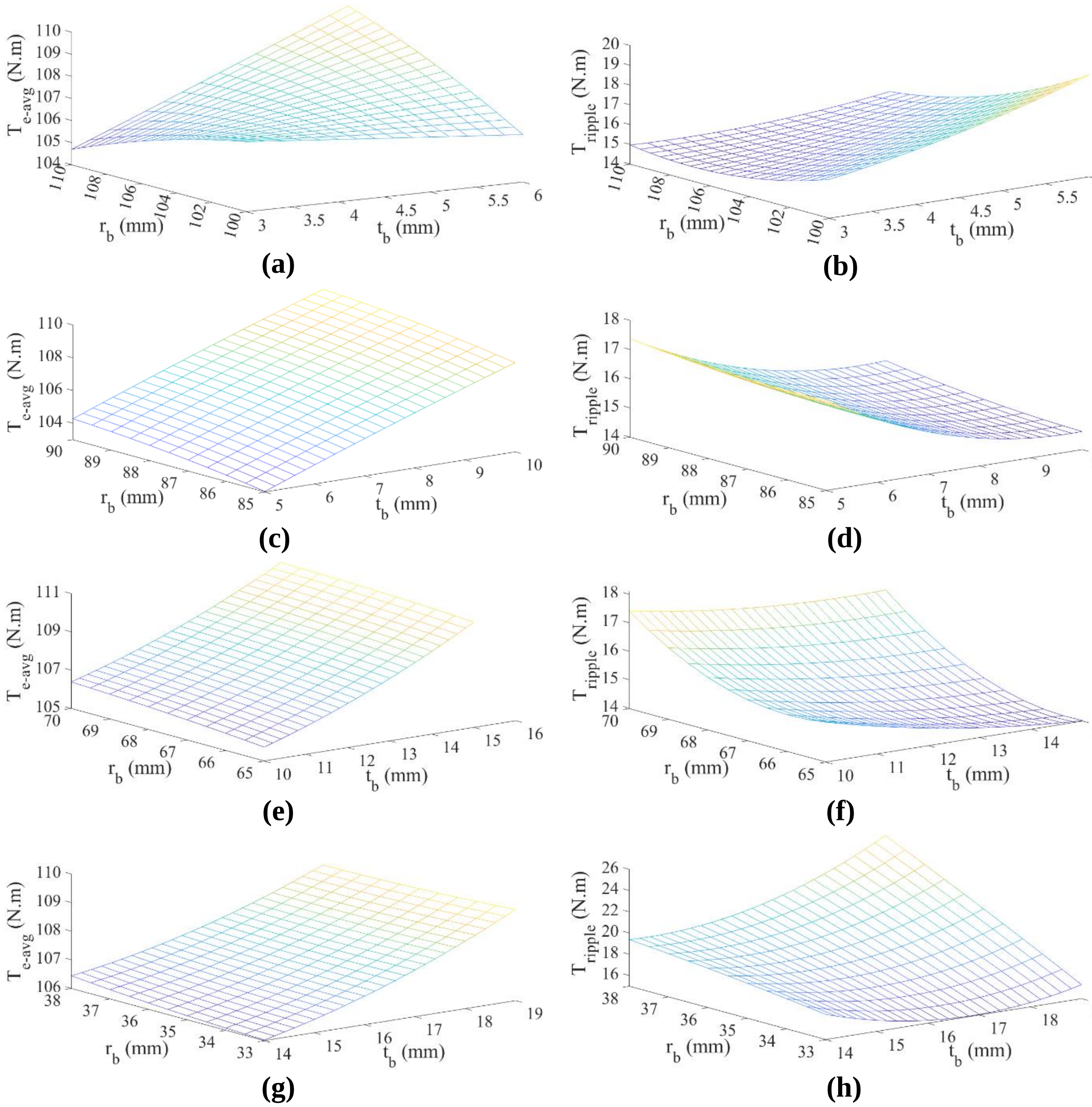

T e-avg (N.m)
r b (mm)
t b (mm)
(a)
T ripple (N.m)
r b (mm)
t b (mm)
(b)
T e-avg (N.m)
r b (mm)
t b (mm)
(c)
T ripple (N.m)
r b (mm)
t b (mm)
(d)
T e-avg (N.m)
r b (mm)
t b (mm)
(e)
T ripple (N.m)
r b (mm)
t b (mm)
(f)
T e-avg (N.m)
r b (mm)
t b (mm)
(g)
T ripple (N.m)
r b (mm)
t b (mm)
(h)

Fig. 17

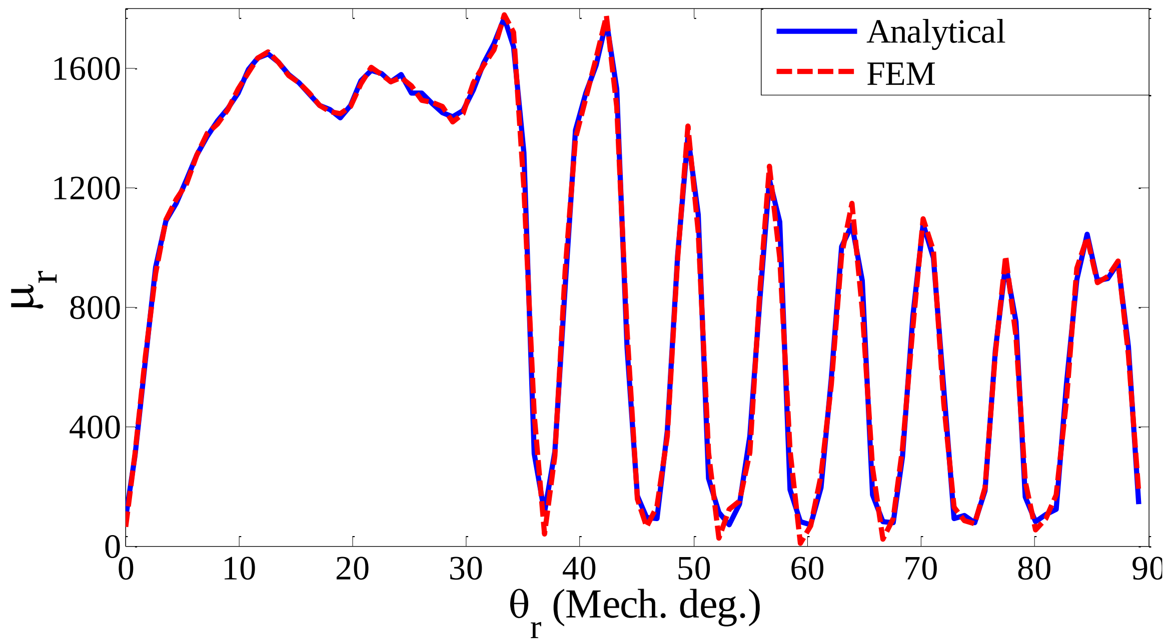

Analytical
FEM
1600
1200
800
400
0
μ_r
0
10
20
30
40
50
60
70
80
90
θ_r (Mech. deg.)

Fig. 18

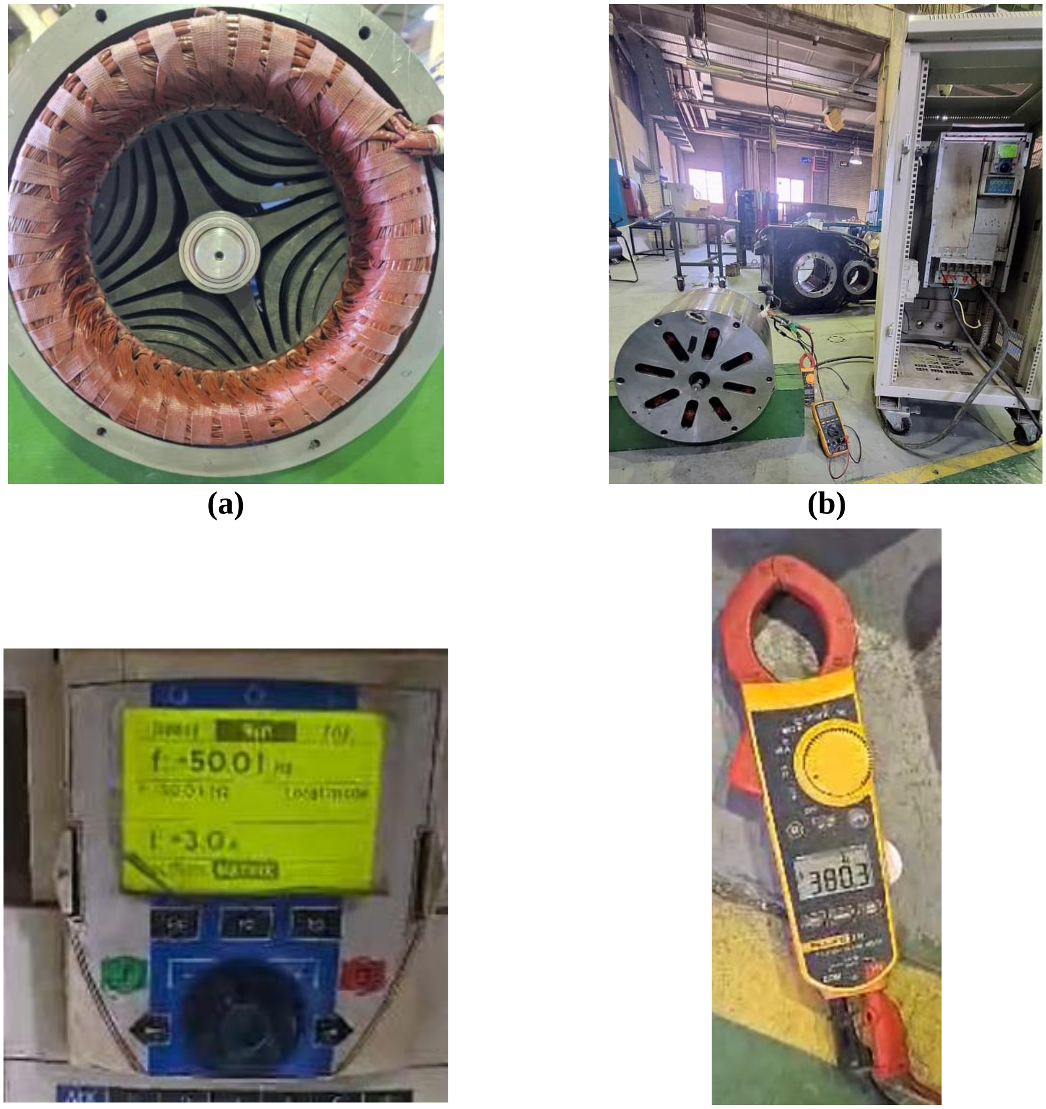

(a) (b)

(c) (d)

Fig. 19

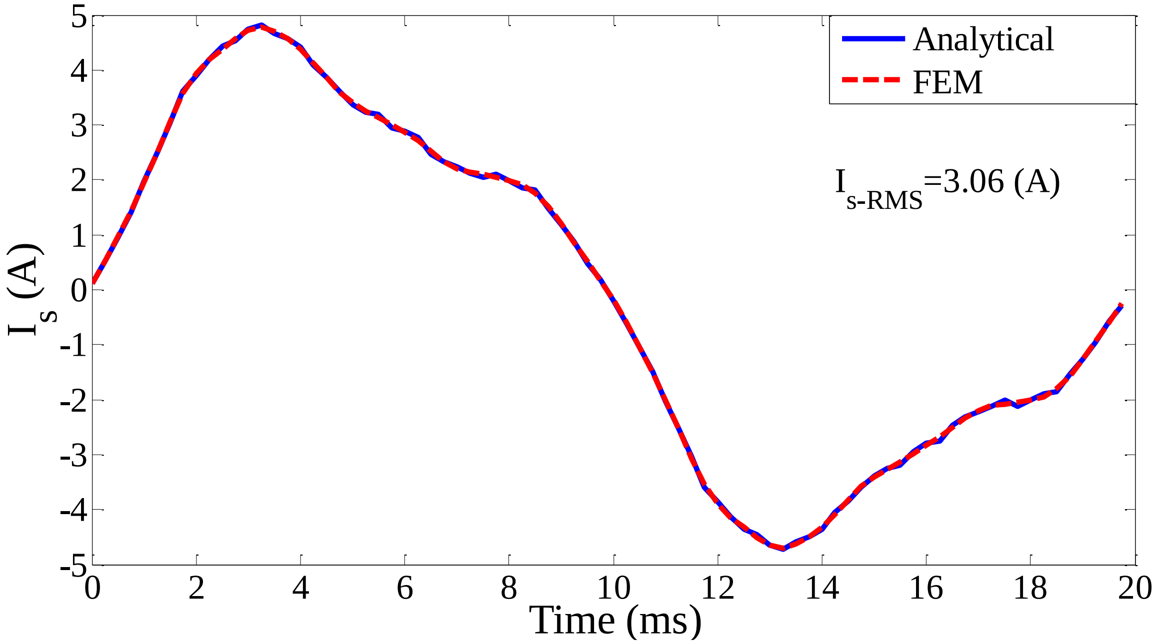

Fig. 20

Table 1

Parameter	**Value**
Rated power	13.5 (kW)
Rated voltage	400 (V)
Stator inner diameter (D_{is})	250 (mm)
Stator outer diameter (D_{os})	360 (mm)
Rotor inner diameter (D_{ir})	50 (mm)
Air-gap length (g)	0.5 (mm)
Axial length (L)	150 (mm)
Number of stator slots	36
Number of coil turns	20 (turn)
Number of poles	4 (poles)
Rated frequency	50 (Hz)

Table 2

Topology	Average value of T_e	Peak-Peak value of T_e
3 flux barriers per pole	108.8 (N.m)	14.9 (N.m)
4 flux barriers per pole	102.4 (N.m)	14.13 (N.m)

Table 3

Phase current	Average value of T_e	Peak-Peak value of T_e
$I_s = 45\ (A)$	108.8 (N.m)	14.9 (N.m)
$I_s = 90\ (A)$	185.5 (N.m)	39.9 (N.m)

Farhad Rezaee-Alam received the B.S. degree from Shahid Chamran University of Ahwaz in 2007, the M.S. and Ph.D. degrees from Khajeh Nasir University of Technology in 2010 and 2015, respectively, all in electrical engineering. He is currently an associate professor in the department of electrical engineering, Lorestan University, Iran. His research interests include design and modeling of electric machines.
E-mail: rezaee.fa@lu.ac.ir

Abbas Nazari Marashi received the B.S. degree in electrical engineering from University of Zanjan, Zanjan, Iran, in 2010, and the M.S. degree in electrical engineering from K. N. Toosi University of Technology, Tehran, Iran, in 2013. He is currently work as a Research assistant in Electrical Machine Research Group, ACECR, K. N. Toosi University of Technology Branch, Tehran, Iran.
E-mail: a_nazari@acecr.ac.ir